Delft University of Technology

Voltage/Current Doubler Converter for Electric Vehicle Wireless Charging Employing Bipolar Pads

Grazian, Francesca; Soeiro, Thiago Batista; Bauer, Pavol

DOI
10.1109/JESTPE.2023.3265402

Publication date
2023

Document Version
Final published version

Published in
IEEE Journal of Emerging and Selected Topics in Power Electronics

Citation (APA)
Grazian, F., Soeiro, T. B., & Bauer, P. (2023). Voltage/Current Doubler Converter for Electric Vehicle Wireless Charging Employing Bipolar Pads. *IEEE Journal of Emerging and Selected Topics in Power Electronics*, *11*(4), 4549-4562. https://doi.org/10.1109/JESTPE.2023.3265402

Important note
To cite this publication, please use the final published version (if applicable).
Please check the document version above.

Copyright
Other than for strictly personal use, it is not permitted to download, forward or distribute the text or part of it, without the consent of the author(s) and/or copyright holder(s), unless the work is under an open content license such as Creative Commons.

Takedown policy
Please contact us and provide details if you believe this document breaches copyrights.
We will remove access to the work immediately and investigate your claim.

This work is downloaded from Delft University of Technology.
For technical reasons the number of authors shown on this cover page is limited to a maximum of 10.

Green Open Access added to TU Delft Institutional Repository

'You share, we take care!' - Taverne project

https://www.openaccess.nl/en/you-share-we-take-care

Otherwise as indicated in the copyright section: the publisher is the copyright holder of this work and the author uses the Dutch legislation to make this work public.

Voltage/Current Doubler Converter for Electric Vehicle Wireless Charging Employing Bipolar Pads

Francesca Grazian, *Graduate Student Member, IEEE*, Thiago Batista Soeiro, *Senior Member, IEEE*, and Pavol Bauer, *Senior Member, IEEE*

***Abstract*— Light-duty electric vehicles (EVs) typically have a rated voltage of either 400 or 800 V. Especially when considering public parking infrastructures or owners with multiple EVs, e.g., car rental companies, EV wireless chargers must efficiently deliver electric power to both battery options. For this purpose, this article proposes an advanced and compact version of the previously defined voltage/current doubler (V/I-D) converter, here comprising two coupled series-compensated bipolar pads (BPPs). The presented system can efficiently charge EVs with both battery voltage classes at the same power level without affecting the current rating of the converter's circuit components. The control scheme is implemented at the power source side in terms of switching frequency and input voltage, and only passive semiconductor devices are employed on board the EV. The equivalent circuit is analyzed, focusing on the BPPs' undesired cross-coupling and its effect on the power transfer. Methods to compensate for the cross-coupling are proposed regarding the BPP design and operating strategy. At 7.2 kW and aligned BPPs, the dc-to-dc efficiency of 96.34% and 96.53% have been measured at 400 and 800 V, respectively. The proposed method has been experimentally validated at different misalignment profiles while considering battery voltages 300–400 V and 600–800 V, which proves that the V/I-D converter is a universal charging solution for EV batteries.**

***Index Terms*— Battery voltage, bipolar pads (BPPs), compensation networks, cross-coupling, electric vehicles (EVs), inductive power transfer (IPT), wireless charging.**

I. Introduction

INDUCTIVE power transfer (IPT) with magnetic resonance coupling has the potential to speed up the transition to electric vehicles (EVs) since it enables a user-friendly charging option: wireless charging. Especially when considering infrastructures that are used by multiple EVs, such as public parking spaces, taxi pickup locations in front of stations or airports, corporate fleets, and car rental or sharing facilities, it is important to ensure that EVs with different nominal battery voltages can be charged efficiently. At the current date, the most common battery voltage ratings are 400 and 800 V [1], [2], [3]. Most EVs use a 400-V architecture since more automotive-qualified components are available for that voltage class. However, some automotive original-equipment manufacturers are moving to 800-V architectures because the higher dc-link voltage results in two main advantages discussed in [3], [4], and [5], being the substantial weight saving across the EV, and possibly the reduction of the battery charging time when using dc-fast charging stations. Examples of automotive companies using 400-V architectures are Audi, Mercedes-Benz, Nissan, Tesla, and Volkswagen. On the other hand, Porsche, KIA, Hyundai, and Aston Martin use 800-V architectures [6].

A power class must be selected when designing an IPT system for light-duty EV wireless charging, limiting the maximum power obtainable from the grid connection. SAE J2954 standard defines three power classes, namely WPT1, WPT2, and WPT3, that correspond to 3.7, 7.7, and 11.1 kVA [7], [8]. It is preferable to fully utilize the available input power when charging EVs that might have either 400- or 800-V battery voltages. In general, the most straightforward solution is to design the IPT system for one of the two battery voltage classes. The same power level is delivered to batteries from the other voltage class through an additional onboard dc/dc converter. In this way, the IPT system would still operate at the same efficiency since the equivalent output load is the same. However, the efficiency of the overall circuit would be impacted by the dc/dc converter required to operate in a wide voltage range. Furthermore, the dc/dc converter adds cost and complexity on board the EV, which is not favorable. Besides the previous work in [9], no other research has been found in the available literature on EV wireless charging systems that can efficiently provide both 400- and 800-V batteries with the same power.

For that purpose, Grazian et al. [9] propose the converter named voltage/current doubler (V/I-D). This novel universal wireless charging solution is suitable for both battery voltage classes. The V/I-D circuit employs two H-bridge inverters connected to the same dc bus, each powering one set of series-compensated coupled coils. The secondary circuits are connected to a rectification stage directly interfaced with the battery. According to Fig. 1, the V/I-D converter employs two primary and two secondary coils, which, in [9], are arranged in two physically separated sets of rectangular coupled coils. Thereby, the distance between these two sets of coupled coils is large enough to eliminate their undesired cross-coupling. In EV wireless charging, this can be achieved by placing one set of coupled coils in correspondence with the back of the EV while the other is installed at the front. In that case, the operation of the V/I-D converter is close to the ideal one.

Manuscript received 17 November 2022; revised 16 February 2023; accepted 28 March 2023. Date of publication 7 April 2023; date of current version 2 August 2023. Recommended for publication by Associate Editor Yi Tang. *(Corresponding author: Francesca Grazian.)*

The authors are with the Department of Electrical Sustainable Energy, Delft University of Technology, 2628CD Delft, The Netherlands (e-mail: F.Grazian@tudelft.nl).

Color versions of one or more figures in this article are available at https://doi.org/10.1109/JESTPE.2023.3265402.

Digital Object Identifier 10.1109/JESTPE.2023.3265402

2168-6777 © 2023 IEEE. Personal use is permitted, but republication/redistribution requires IEEE permission.
See https://www.ieee.org/publications/rights/index.html for more information.

Authorized licensed use limited to: TU Delft Library. Downloaded on August 21,2023 at 13:07:11 UTC from IEEE Xplore. Restrictions apply.

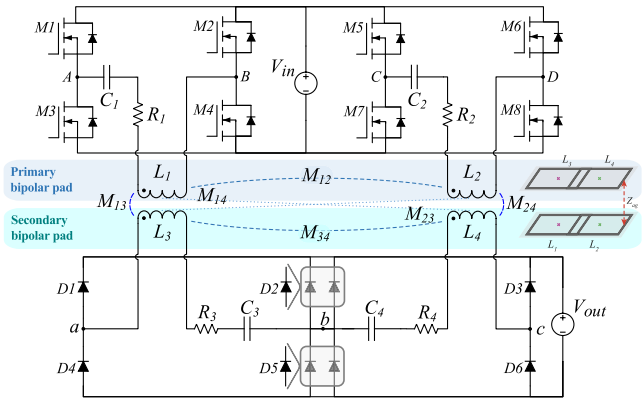

Fig. 1. V/I-D converter for IPT systems employing series-compensated BPPs. Herein, $D2$ and $D5$ can be advantageously assembled with two parallel diodes of the same technology used in $D1$, $D3$, $D4$, and $D6$. In this case, the current rating of the converter's circuit components is similar for a given charging power independently of the voltage or current doubling operation.

However, this solution might not be practical since it does not give much freedom in mounting the IPT system, which could be significantly limiting for small-size light-duty EVs. On the other hand, the use of multicoil pads would provide a compact magnetic configuration for the V/I-D converter's coupled coils because, in that case, the two coils at each circuit side are deployed on the same ferrite layer. This implementation has a greater industrial value since it eases the installation on the IPT charging station and onboard the EV. In EV wireless charging applications, the most common multicoil pads are the bipolar pads (BPPs) [10] and the double-D quadrature pad (DDQP) [11]. Considering the symmetrical structure of the V/I-D converter, employing BPPs is preferable given the symmetry between the two rectangular coils in each BPP, as qualitatively shown in Fig. 1. This symmetry is not intrinsic to DDQPs, making them unsuitable for the V/I-D converter.

This article proves the feasibility of employing two coupled BPPs as the magnetic arrangement of the V/I-D converter. This implementation intrinsically results in cross-coupling due to the proximity between the two sets of coupled coils, which certainly affects the power transfer of the V/I-D converter. This means that the design guidelines and operating scheme proposed in [9] are not suitable for the V/I-D converter using BPPs. The main contributions of this article are as follows.

1) Overview of BPPs in the available literature is providing insights into their main features and use. In this article, a primary BPP is coupled with a secondary BPP, which is not common in the literature since BPPs are mostly used at the primary or secondary circuit.
2) Investigation of the effects of the BPP unwanted cross-coupling on the V/I-D converter's functionality; definition of the operating scheme and the design requirements for the coupled BPPs to mitigate the cross-coupling effects on the power transfer.
3) Experimental proof that the proposed V/I-D converter employing BPPs can achieve high power transfer efficiency when charging both 400 and 800 V at the same power level. At the output power of 7.2 kW and aligned BPPs, the dc-to-dc efficiency of 96.34% and 96.53% have been measured at 400 and 800 V, respectively.
4) Experimental proof of the V/I-D converter's functionality under different misalignment and load conditions typical of EV wireless charging. Battery voltage ranges 300–400 V and 600–800 V have been considered, proving the V/I-D converter is a universal charging solution and not only strictly for 400- and 800-V battery voltages.

It must be noted that the proposed V/I-D converter fundamentally differs from the voltage and current doubling circuits conventionally used in the rectification stage of resonant converters [12]. In general, those circuits limit some components' voltage or current stress, easing their design and implementation. Voltage and current doubling circuits have also been used in IPT systems. For instance, voltage doubler rectifying circuits are employed when the output voltage is considerably greater than the input voltage [13]. On the other hand, it is advantageous to adopt current doubler rectifying circuits in IPT systems with a large output current, as explained in [14], [15], and [16]. However, these conventional doubling circuits have a fixed voltage or current gain optimized for the specific IPT application.

Conversely, the voltage and the current gains of the proposed V/I-D converter are not fixed since 400- and 800-V batteries can be directly charged at the same power level. This means that the V/I-D converter has a selective output doubling behavior depending on the modulation of the H-bridge inverters. The operation can assume either the voltage doubler mode (suitable for 800-V batteries) or the current doubler mode (suitable for 400-V batteries).

The remaining sections of the article are organized as follows. Section II discusses the operating scheme and the analytical circuit modeling of the V/I-D converter. The main features and challenges due to the undesired cross-coupling of the BPPs are explored in Section III, focusing on the effects on the power transfer. Based on those results, the BPPs are designed through finite element method (FEM) analysis and then implemented. After that, Section IV describes the 7.7-kW laboratory prototype used to verify the functionality of the proposed V/I-D converter. The expected operating points depending on the receiver pad's misalignment are analyzed from the analytical model. The experimental results in terms of dc-to-dc efficiency and circuit waveforms can be found in Section V for both aligned and misaligned BPPs. Finally, conclusions are provided in Section VI.

II. V/I-D Converter

A. Concept and Ideal Operating Scheme

The power transfer control of the V/I-D converter in Fig. 1 is executed at the primary circuits and depends on the H-bridge inverters' modulation. For instance, when the two inverters work in phase at 50% duty cycle as illustrated in the equivalent circuit in Fig. 2(a), the current flowing through the two primary coils has the same direction. As a consequence of this modulation, the secondary coils result in an equivalent series connection. This means that they share the same nominal current, which makes this operation suitable for 800-V batteries. On the other hand, when the two inverters are 180° out of phase at 50% duty cycle, as illustrated in the equivalent circuit in Fig. 2(b). This translates into an

Authorized licensed use limited to: TU Delft Library. Downloaded on August 21,2023 at 13:07:11 UTC from IEEE Xplore. Restrictions apply.

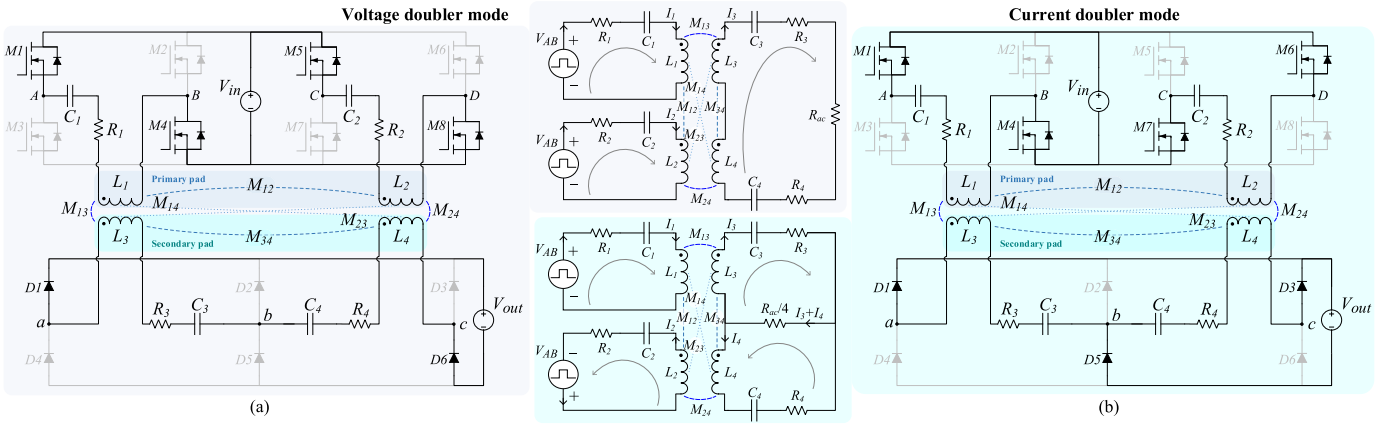

Fig. 2. Equivalent circuit of the V/I-D converter when operating as (a) voltage doubler (suitable for 800-V batteries) and (b) current doubler (suitable for 400-V batteries), which are described by (1) and (2), respectively. The semiconductor devices that conduct during the positive half-wave of v_{AB} are highlighted.

equivalent parallel connection of the secondary coils. Consequently, this modulation results in a load current doubling the coils' nominal current making this operation suitable for 400-V batteries. The strength of the proposed V/I-D converter is that each component ideally has the same power loss in the two operating modes since they are conducting the same amount of current. There is only a slight difference between the two power transfer efficiencies because double the number of diodes is conducted in the current doubler mode.

B. Analytical Modeling

The equivalent frequency-domain circuit in Fig. 2(a) of the voltage doubler mode is described by the Kirchhoff voltage law in (1), as shown at the bottom of the page, while the one in Fig. 2(b) of the current doubler mode is described by (2), as shown at the bottom of the page. Thereby, $\boldsymbol{V}_{AB}$ is taken as reference according to the phasor convention, and it is defined in (3) through the first-harmonic approximation [17]. The battery and power handling are replaced by the equivalent first-harmonic load R_{ac} in (4). The impedance $\boldsymbol{Z_i}$ of each resonant circuit is defined in (5). The mutual inductance M_{ih} is expressed in (6) in terms of the coupling factor k_{ih}, where M_{13} and M_{24} are the main mutual inductances functional to the operation of the V/I-D converter. On the other hand, M_{12} and M_{34} are due to the cross-coupling present between the two coils of each BPP, while M_{14} and M_{23} are due to the diagonal cross-coupling between two coupled BPPs. Moreover, the power transfer efficiency can be calculated as explained in [9]

$$\boldsymbol{V}_{AB} = V_{AB,1} = V_{AB}\underline{/0^\circ} = \frac{4}{\pi}V_{in} \quad V_{CD} = V_{AB} \tag{3}$$

$$R_{ac} = \frac{8}{\pi^2}\frac{V_{out,max}^2}{P_{out}} \tag{4}$$

$$\boldsymbol{Z_i} = R_i + j\omega X_i, \quad X_i = \omega L_i - \frac{1}{\omega C_i} : \ i = 1, \ldots, 4 \tag{5}$$

$$M_{ih} = M_{hi} = k_{ih}\sqrt{L_i L_h} : \ i, h = 1, \ldots, 4 \wedge i \neq h. \tag{6}$$

The V/I-D converter would assume the intended operation explained in Section II-A when the unwanted cross-coupling between the coupled coils is not present. This is the case of the implementation in [9], where the two sets of coupled coils are placed far from each other. However, when considering coupled BPPs as the magnetic arrangement, cross-coupling is inevitable to a certain extent. From (1), it is possible to notice that all instances of mutual inductance due to the coils' cross-coupling add up to the main functional mutual inductance. This is because the currents have the same direction in the voltage doubler mode, as shown in Fig. 2(a). In contrast, Fig. 2(b) shows that the currents have opposite directions at each circuit side in the current doubler mode. This justifies the negative signs in (2) associated with all the mutual inductances due to the cross-coupling. Therefore, the cross-coupling effects on the V/I-D converter's power transfer must be investigated to evaluate whether the operating scheme defined in Section II-A would still be valid.

$$\begin{bmatrix} \boldsymbol{V}_{AB} \\ \boldsymbol{V}_{CD} \\ 0 \\ 0 \end{bmatrix} = \begin{bmatrix} \boldsymbol{Z_1} & j\omega M_{12} & j\omega(M_{13}+M_{14}) & 0 \\ j\omega M_{12} & \boldsymbol{Z_2} & j\omega(M_{23}+M_{24}) & 0 \\ j\omega(M_{13}+M_{14}) & j\omega(M_{23}+M_{24}) & (\boldsymbol{Z_3}+\boldsymbol{Z_4}+R_{ac}+2j\omega M_{34}) & 0 \\ 0 & 0 & 1 & -1 \end{bmatrix} \begin{bmatrix} \boldsymbol{I_1} \\ \boldsymbol{I_2} \\ \boldsymbol{I_3} \\ \boldsymbol{I_4} \end{bmatrix} \tag{1}$$

$$\begin{bmatrix} \boldsymbol{V}_{AB} \\ \boldsymbol{V}_{CD} \\ 0 \\ 0 \end{bmatrix} = \begin{bmatrix} \boldsymbol{Z_1} & -j\omega M_{12} & j\omega M_{13} & -j\omega M_{14} \\ -j\omega M_{12} & \boldsymbol{Z_2} & -j\omega M_{23} & j\omega M_{24} \\ j\omega M_{13} & -j\omega M_{23} & \left(\boldsymbol{Z_3}+\frac{R_{ac}}{4}\right) & \left(-j\omega M_{34}+\frac{R_{ac}}{4}\right) \\ -j\omega M_{14} & j\omega M_{24} & \left(-j\omega M_{34}+\frac{R_{ac}}{4}\right) & \left(\boldsymbol{Z_4}+\frac{R_{ac}}{4}\right) \end{bmatrix} \begin{bmatrix} \boldsymbol{I_1} \\ \boldsymbol{I_2} \\ \boldsymbol{I_3} \\ \boldsymbol{I_4} \end{bmatrix} \tag{2}$$

Authorized licensed use limited to: TU Delft Library. Downloaded on August 21,2023 at 13:07:11 UTC from IEEE Xplore. Restrictions apply.

III. Bipolar Pads

A. Overview: BPP as a Magnetic Coil Arrangement

The BPP consists of two independent partially overlapped rectangular coils. It was first introduced in [10] to implement a versatile EV transmitting pad that, depending on the phase of the current flowing through each coil, can work as a polarized or nonpolarized pad. Consequently, the BPP has high interoperability since it has relatively strong magnetic coupling with polarized pads such as double-D pads (DDPs) and nonpolarized pads such as circular or rectangular pad. Other examples of the BPP employed as a transmitting pad for interoperability can be found in [18], [19], [20], [21], and [22]. On the other hand, the authors [23], [24], [25] explore the advantages of using the BPP as receiving pad. In all these studies, the two coils in the same BPP are magnetically decoupled by appropriately selecting their overlap such that their concatenated magnetic flux approximates zero. As explained in [23], this overlapping area depends on the structure of the BPP itself and also on the configuration of the pad with which the BPP is coupled. Therefore, the overlapping area is generally chosen from the analysis of the pads through the FEM.

However, when the BPP is used as both the transmitting and receiving pads, the cross-coupling between the coils placed at the diagonal opposite sides of the circuit would be present. Referring to Fig. 1, this cross-coupling is denoted by M_{14} and M_{23}. Previous research has not extensively explored the use of coupled BPPs and their cross-coupling. In [26], it has been shown that it is possible to minimize the diagonal cross-coupling by enlarging the overlapping area at the cost of reintroducing the cross-coupling between the coils on the same BPP. This solution might be beneficial since, as shown in [25] and [27], the cross-coupling on the same BPP is relatively constant over the misalignment, which means that its effect could be compensated by adding extra compensation capacitance in the resonant circuit [25], [28], [29].

B. Analysis: Influence of BPPs' Cross-Coupling on the V/I-D Converter's Functionality

Understanding how the cross-coupling within the same BPP and the diagonal cross-coupling between opposite BPPs influence the power transfer of the V/I-D converter is fundamental to assessing which of the two must be minimized by adequately designing the BPPs.

1) Assumptions: The influence of the cross-coupling has been evaluated analytically for the two operating modes from (1) and (2), considering the input parameters listed in Table I. Thereby, the main mutual inductance M has been computed from (7) considering the three possible values of $f_0 = (\omega_0/2\pi)$. The operating frequency of the H-bridge inverters $f_{sw} = f_0$ is constrained in the range allowed by SAE J2954, i.e., 79, ..., 90 kHz. To keep the analysis generic, no specific values have been chosen for the coils' inductance and the compensation capacitances. The secondary circuits are considered in resonance, i.e., $X_3 = X_4 = 0$. Consequently, the impedance of the secondary circuit results in $\boldsymbol{Z_3} = \boldsymbol{Z_4} = R$. In contrast, the primary circuits are slightly inductive ($X_1 = X_2 > 0$) to ensure the ZVS turn-on of the H-bridge inverters. As a result, the impedance of the primary circuits is $\boldsymbol{Z_1} = \boldsymbol{Z_2} = R + jX$. In addition, the diagonal cross-coupling from the opposite BPP and the cross-coupling within the same BPP have been studied separately to isolate their characteristics. Each of them has been swept such that $M_{\text{cross}} = [1/10, 1/8, 1/6, 1/4, 1/3, 1/2] \cdot M$, while the main mutual inductances are defined as $M_{13} = M_{24} = M$

TABLE I
Input Parameters Used in the Analysis of Section III-B

Parameter	Definition	Value
P_{out}	Nominal output power	7.2 kW
V_{out}	Nominal output voltage	[400, 800]V
V_{in}	Input voltage	360...500 V
f_0	Circuit resonant frequency	[79, 85, 90] kHz
M	Main mutual inductance	[77.24, 81.79, 88.00] μH
R	Circuit equivalent resistance	0.5 Ω
X	Circuit equivalent reactance	5 Ω

$$M = \frac{8}{\pi^2}\frac{V_{\text{in}}V_{\text{out}}}{\omega_0 P_{\text{out}}}. \tag{7}$$

In this analysis and the one of Section IV-B, the primary currents are computed considering the inverted output voltage from their respective H-bridge inverter as a reference. For instance, $\boldsymbol{I_1}$ has been computed with respect to $\boldsymbol{V}_{\text{AB}}$, while $\boldsymbol{I_2}$ takes $\boldsymbol{V}_{\text{CD}}$ as a reference.

2) Analysis: Fig. 3 compares the effects of the cross-coupling to the case in which $M_{\text{cross}} = 0 \cdot M$. The comparison is made in terms of the amplitude and the phase angle of the primary currents $\boldsymbol{I_1}$ and $\boldsymbol{I_2}$, and the output current I_{out}.

Fig. 3(a) shows that the diagonal cross-coupling between opposite BPPs ($M_{\text{cross}} = M_{14} = M_{23}$) would still lead to inductive primary currents. However, compared with the case with no cross-coupling, the primary currents would be more inductive in the current doubling mode, while they would be less inductive in the voltage doubling mode. The diagonal cross-coupling would either add up or reduce the main mutual inductance, which is particularly clear from (1) and (2). Because this cross-coupling directly influences the power transfer, it is not possible to compensate for it by modifying the value of the compensation capacitances. Nevertheless, it is reasonable to consider M_{cross} acceptable if $M_{\text{cross}} \leq 1/4 \cdot M$ because, within this range, the variation in I_{out} can be counteracted by stepping up V_{in}. Moreover, in this range, the phase angle of the primary currents in both modes would be enough to guarantee the ZVS turn-on of the two H-bridge converters with the moderated amount of reactive current.

Similarly, Fig. 3(b) shows that the cross-coupling within the same BPP ($M_{\text{cross}} = M_{12} = M_{34}$) would still lead to inductive primary currents. The variation trend in the two operating modes is similar to Fig. 3(a). However, when considering $|I_1|$, $|I_2|$, and I_{out}, it is possible to notice that, for the same range of M_{cross}, the variations are more limited than in Fig. 3(a). This means that it is possible to tolerate higher values of M_{cross} and compensate for their effects by stepping down V_{in}. Since, in this case, the cross-coupling is present within each BPP,

Authorized licensed use limited to: TU Delft Library. Downloaded on August 21,2023 at 13:07:11 UTC from IEEE Xplore. Restrictions apply.

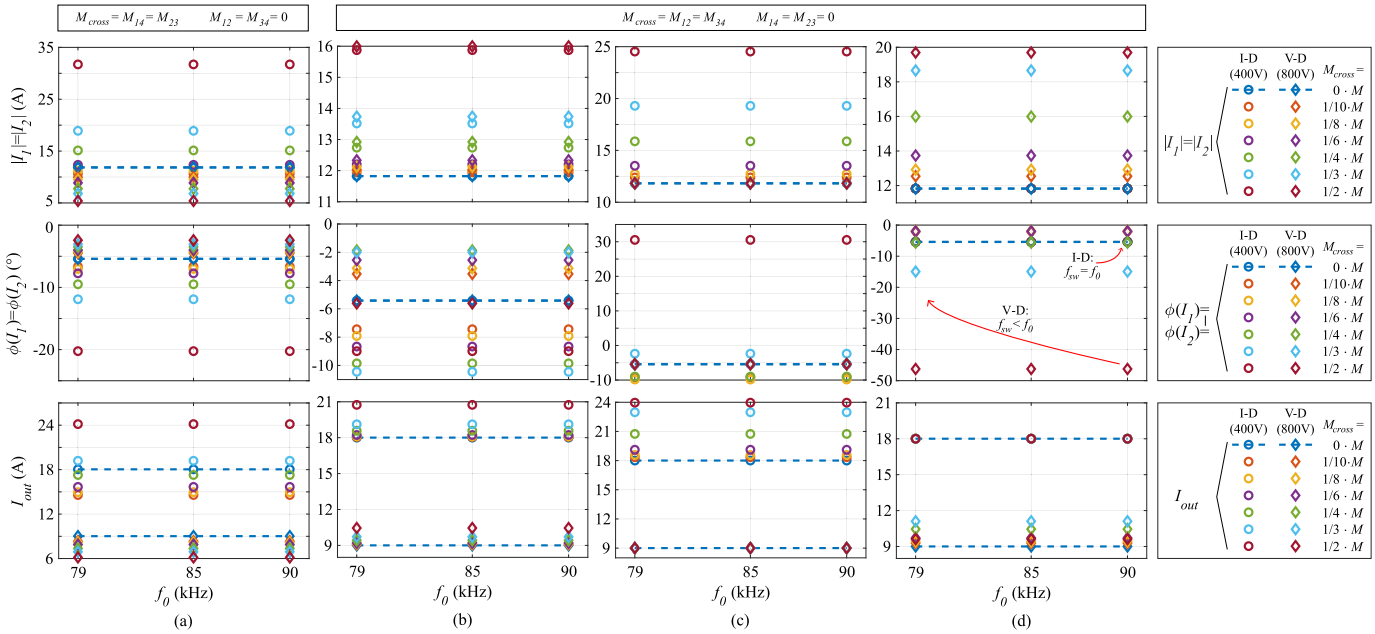

Fig. 3. Influence of the cross-coupling M_{cross} in both operating modes of the V/I-D converter in Fig. 1. The analysis is made in terms of the amplitude and the phase angle of the primary currents, being $|I_1| = |I_2|$ and $\phi(I_1) = \phi(I_2)$, and the dc output current I_{out} for different values of M_{cross}, such that $M_{\text{cross}} = [0, 1/10, 1/8, 1/6, 1/4, 1/3, 1/2] \cdot M$. (a) Effects of the diagonal cross-coupling from opposite BPPs ($M_{\text{cross}} = M_{14} = M_{23}$). (b)–(d) Effects of the cross-coupling within the same BPP ($M_{\text{cross}} = M_{12} = M_{34}$). (c) Mitigation of M_{cross} in the voltage doubler (V-D) mode by turning all compensation capacitances according to (8). (d) Mitigation of M_{cross} in the current doubler (I-D) mode by turning all compensation capacitances according to (9).

it does not directly influence the power transfer between the primary and the secondary circuits. Its effects stay isolated on the two sides, and they can be treated as an extra impedance with either an inductive or capacitive nature, as shown in (1) and (2), respectively. This means that the contribution of M_{12} and M_{34} can be considered and eliminated in one of the two operating modes by selecting a suitable compensation capacitance. Examples of M_{12} and M_{34} compensation are discussed in Fig. 3(c) and (d).

In Fig. 3(c), the cross-coupling within the same pad is compensated for the voltage doubler mode, and its impact on the current doubler mode is analyzed. This has been performed for all values of M_{cross} by adding an extra reactance to $\boldsymbol{Z_i}$ as shown in (8), which translates into a lower value of the compensation capacitance

$$\text{V-Doubler}\begin{cases} \boldsymbol{Z_i} = R + j\left(X - \omega_0 M_{\text{ih}} \dfrac{|I_h^*|}{|I_i^*|}\right) \\ \rightarrow C_i = \dfrac{1}{\omega_0\left[\omega_0\left(L_i + M_{\text{ih}}\dfrac{|I_h^*|}{|I_i^*|}\right) - X\right]} \\ i, h = 1, \ldots, 4: \\ i = 1 \Leftrightarrow h = 2, \quad i = 2 \Leftrightarrow h = 1 \\ i = 3 \Leftrightarrow h = 4, \quad i = 4 \Leftrightarrow h = 3. \end{cases} \tag{8}$$

In (8), $|I_i^*|$ and $|I_h^*|$ indicate the current amplitudes that would result from the case with no cross-coupling, i.e., $M_{\text{cross}} = 0$, which can be computed from (1). As expected, the operation of the voltage doubling mode with cross-coupling within the same BPP coincides with the operation in the ideal case with no cross-coupling. On the other hand, with the same circuit parameters, the operation in the current doubling mode could result in the hard-switching of the H-bridge inverters if $M_{\text{cross}} > 1/3 \cdot M$.

In Fig. 3(d), the cross-coupling within the same pad is compensated for the current doubler mode, and its impact on the voltage doubler mode is analyzed. In this case, an extra reactance has been added to $\boldsymbol{Z_i}$ as shown in (9) for all values of M_{cross}, which would translate into a higher value of the compensation capacitance.

As expected, the operation in the current doubling mode with the cross-coupling within the same BPP coincides with the operation in the ideal case with no cross-coupling. The voltage doubling mode operation with the same circuit parameters would result in a highly inductive primary current if $M_{\text{cross}} > 1/3 \cdot M$. In that case, the power transfer efficiency would be lower due to the circulating reactive power and the relatively large turn-off current point. Nevertheless, the ZVS turn-on of the H-bridges is maintained, which would not be the case in Fig. 3(c)

$$\text{I-Doubler}\begin{cases} \boldsymbol{Z_i} = R + j\left(X + \omega_0 M_{\text{ih}} \dfrac{|I_h^*|}{|I_i^*|}\right) \\ \rightarrow C_i = \dfrac{1}{\omega_0\left[\omega_0\left(L_i - M_{\text{ih}}\dfrac{|I_h^*|}{|I_i^*|}\right) - X\right]} \\ i, h = 1, \ldots, 4: \\ i = 1 \Leftrightarrow h = 2, \quad i = 2 \Leftrightarrow h = 1 \\ i = 3 \Leftrightarrow h = 4, \quad i = 4 \Leftrightarrow h = 3. \end{cases} \tag{9}$$

3) Chosen Cross-Coupling Compensation and Operating Strategy: The results from Fig. 3 make it preferable to minimize the diagonal cross-coupling (M_{14} and M_{23}) by properly designing the overlap area of the coils within the same BPP.

Authorized licensed use limited to: TU Delft Library. Downloaded on August 21,2023 at 13:07:11 UTC from IEEE Xplore. Restrictions apply.

TABLE II
GIVEN DIMENSIONS VALID FOR BOTH BPPS REFERRING TO FIG. 4

Parameter	Definition	Value (mm)
x_a, y_a, z_a	Aluminum plate's dimensions	570, 370, 2
x_f, y_f, z_f	Ferrite layer's dimensions	559, 364, 4.1
x_l	Coils' total length	545
y_c	Coils' width	350
$z_{f\text{-}c1}$, $z_{f\text{-}c2}$	Ferrite and coils air gap	3, 10.5
$z_{f\text{-}a}$	Ferrite and aluminum air gap	4
C_{sp}	Total coil's spread	65
d	Litz wire's external diameter	2.5
$x_{f,unit}$, $y_{f,unit}$	Ferrite unit's dimensions	43, 28
Ferrite unit: 3C95, PLT43/28/4.1; Litz wire: 600x0.071mm		

This choice cannot guarantee that the cross-coupling within the same BPP (M_{12} and M_{34}) is negligible. However, adequate compensation capacitance selection can compensate for its effect on the power transfer. From the previous analysis, it has been found that it is preferable to tune the compensation capacitances in the current doubler mode through (9). The tuning of the capacitors and the H-bridge inverters' switching frequency is performed at $f_{\text{sw}} = f_0 = 90$ kHz in the current doubler mode. This guarantees that, by operating the inverters at $f_{\text{sw}} = 79$ kHz during the voltage doubler mode, the primary currents would be less inductive, reducing the circulating reactive power and the turn-off current point that can be problematic as shown in Fig. 3(d) if $M_{\text{cross}} > 1/3 \cdot M$. This tuning and operating strategy are qualitatively shown in Fig. 3(d). Thereby, the resulting primary currents' phase angle at 79 kHz in the voltage doubler mode cannot be computed since, in this analysis, the circuits' impedance $\boldsymbol{Z_i}$ are defined just for the resonant frequency. The advantage of this operating scheme will be proved in Section IV-B. In addition, by choosing $f_0 = 90$ kHz, the required mutual inductance M is the lowest value in Table I, which eases the requirement on the nominal coupling. It must be noted that these design and operating strategies are essentially different from the V/I-D converter previously proposed in [9], which resembled the ideal operating scheme.

C. Design: Cross-Coupling Sensitivity Analysis Through FEM

The coupled BPPs must be designed according to the cross-coupling analysis of Section III-B, such that the following holds.

1) The nominal M_{13} and M_{24} are in the range of 77.24 μH.
2) The diagonal cross-coupling M_{14} and M_{23} between the two BPPs are negligible at the aligned position and for the nominal air gap. This results from selecting the overlap area between the two coils within each BPP.

The chosen BPP geometry is illustrated in Fig. 4 of which given dimensions are listed in Table II. The dimensions of the aluminum shield, the ferrite plate, and the outer sides of the winding area are chosen, given by the available physical space for the wireless charging system. In addition, each winding consists of several turns of the chosen Litz wire having d as the external diameter. For simplicity, the windings are modeled

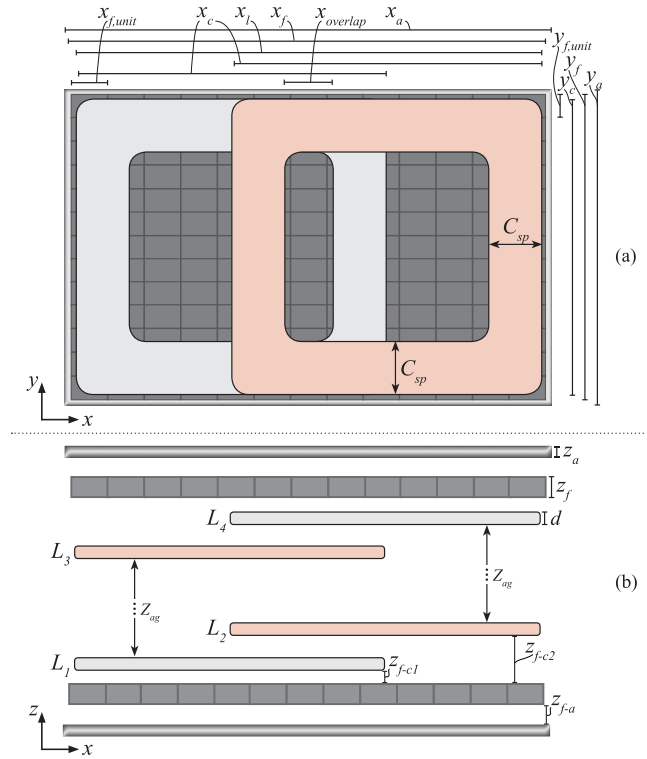

Fig. 4. Structure and geometry of the coupled BPPs viewed from (a) xy plane and (b) xz plane.

as a massive planar conductor of which the total coil's spread C_{sp} is defined in Fig. 4. Even though C_{sp} is considered to be fixed as specified by Table II, there is still room to select the number of turns of each coil. In particular, this choice must guarantee the below.

1) $M_{13} \approx M_{24} \approx 77.24$ μH is satisfied while the air gap between the two BPPs is $Z_{\text{ag}} \approx 100$ mm.
2) The two coils within each BPP have similar parameters aiming for a symmetrical design.
3) The conduction losses in the primary and secondary circuits are equal.

The number of turns of each coil satisfying the above-mentioned requirements is summarized in Table III. These have been found through the FEM analysis of the coupled BPPs with an initial overlap of $x_{\text{overlap}} = 0$. It can be noticed that the coil placed closer to the ferrite in each BPP has one less turn. This choice guarantees similarity between the two self-inductance values and also between M_{13} and M_{24} considering the uneven placement of the coils in the z-direction as shown in Fig. 4(b). The initially selected C_{sp} would be enlarged if it cannot accommodate the necessary number of turns that satisfies the requirements on the BPPs.

After selecting the number of turns, the overlap area between the two coils in the same pad must be chosen, which, in Fig. 4, is defined in terms of x_{overlap}. The value of x_{overlap} must result in a negligible diagonal cross-coupling. From the cross-coupling analysis in Fig. 3, that is the case if M_{14} and M_{23} are at maximum $(1/10) \cdot M$, where $M \approx M_{13} \approx M_{24}$. According to (10), x_{overlap} can be expressed as a function of the single coil's length x_c. In this analysis, C_{sp} and the total length occupied by the coils x_l are considered to be fixed,

Authorized licensed use limited to: TU Delft Library. Downloaded on August 21,2023 at 13:07:11 UTC from IEEE Xplore. Restrictions apply.

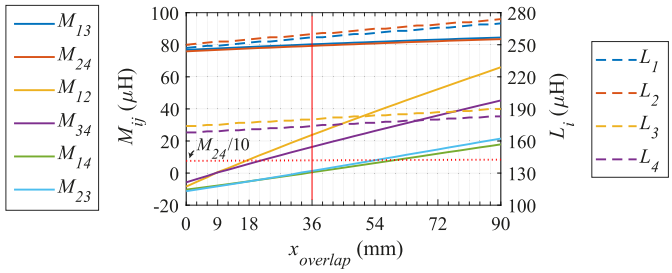

Fig. 5. Self-inductances and mutual inductances of the coupled BPPs depending on x_{overlap} resulting from the FEM analysis.

TABLE III
RESULTING BPP PARAMETERS FROM THE ANALYSIS OF SECTION III-C

Parameter	Definition	Value
N_1	Number of turns used for L_1	17 p.u.
N_2	Number of turns used for L_2	18 p.u.
N_3	Number of turns used for L_3	15 p.u.
N_4	Number of turns used for L_4	14 p.u.
x_c	Single coil's length	355.5 mm
$x_{overlap}$	Coils' overlap in each BPP	36 mm

which values are listed in Table II. On the other hand, x_c and x_{overlap} can vary in the range specified by (11)

$$x_{\text{overlap}}(x_c) = 2 \cdot x_c - 2 \cdot C_{\text{sp}} - x_l \tag{10}$$

$$x_c = \left[\frac{x_l}{2} + C_{\text{sp}};\ x_l\right] \rightarrow x_{\text{overlap}} = \left[0;\ x_l - 2 \cdot C_{\text{sp}}\right]. \tag{11}$$

Several coupled BPPs configurations have been created by sweeping x_{overlap} in the range $0, \ldots, 90$ mm every 3 mm equally for both BPPs. At the same time, the self-inductance and the mutual inductance of all the coils are assessed through the FEM analysis considering $Z_{\text{ag}} = 101.5$ mm. These results are summarized in Fig. 5.

It must be noted that the cross-coupling within the same pads M_{12} and M_{34} is minimized when $x_{\text{overlap}} = 9$ mm. On the other hand, the diagonal cross-coupling between opposite pads M_{14} and M_{23} is minimum for a greater value of x_{overlap}, being 36 mm. This result coincides with the analysis performed in [26]. The coupled BPPs with $M_{14} \approx M_{23} \approx 0$ are preferable since they result in a V–I/D converter operation close to the ideal case. Therefore, the values of x_{overlap} and x_c listed in Table III are selected for the BPP design. Nevertheless, if 36 mm $\leq x_{\text{overlap}} \leq$ 54 mm, M_{14} and M_{23} can be considered negligible given the analysis performed in Fig. 3(a).

In addition, Fig. 5 shows that all four cross-coupling mutual inductances are negative when there is no overlap between the coils, i.e., $x_{\text{overlap}} = 0$. The physical meaning of these results can be understood by analyzing the magnetic field generated by the coils. An example is shown in Fig. 6(a) considering two coupled BPPs with $x_{\text{overlap}} = 0$. A current flows through the coil with inductance L_1 generating a magnetic field along the positive z-axis. The sign of the mutual inductance to a coupled coil depends on the direction of the total concatenated magnetic flux. For instance, the magnetic flux linking to the coil with inductance L_3 is positive since it has the same direction of the $+z$-axis. This translates into $M_{13} > 0$. On the other hand, a negative magnetic flux concatenates to the two coils with inductances L_2 and L_4 resulting in negative cross-coupling mutual inductances, i.e., $M_{12} < 0$ and $M_{14} < 0$. The influence of a negative mutual inductance on the power transfer is discussed in Section IV-B.

On the other hand, Fig. 6(b) shows that a positive flux might link to all three coupled coils when the two coils within each BPP are overlapped, which, according to Fig. 5, that is the case for $x_{\text{overlap}} > 36$ mm.

TABLE IV
MEASURED COILS' PARAMETERS REFERRING TO THE CIRCUIT IN FIG. 1, FOR AN AIR GAP OF $Z_{\text{ag}} = 95$ mm

Parameter	Definition	Value
	Inductance and resistance of:	
L_1, R_1	the primary BPP	252.5 μH, 620 mΩ
L_2, R_2		250.4 μH, 600 mΩ
L_3, R_3	the secondary BPP	167.0 μH, 520 mΩ
L_4, R_4		161.8 μH, 500 mΩ
	Mutual inductance due to:	
M_{13}, M_{24}	the main functional coupling	80.3 μH, 76.8 μH
M_{12}, M_{34}	the cross-coupling within the BPP	30.1 μH, 17.7 μH
M_{14}, M_{23}	the diagonal cross-coupling	5.6 μH, 6.7 μH

D. Implementation: Coupled BPPs for the V/I-D Converter

The coupled BPPs design with the minimum diagonal cross-coupling identified in Section III-C has been implemented. The overall parameters of the resulting BPPs are plotted in Fig. 7, where the reference coordinate is chosen with respect to the implemented BPPs in Fig. 8. The parameters of the coupled BPPs in the aligned position are listed in Table IV. It can be noticed that M_{13} and M_{24} differ by less than 4% from the target main mutual inductance of 77.24 μH. Even though the resulting diagonal cross-coupling M_{14} and M_{23} are larger than the values expected from Fig. 5, these are still acceptable since they are lower than $(1/10) \cdot M_{24}$. This discrepancy is due to the manufacturing tolerances and nonidealities of the materials used for the pads' structure.

Fig. 7 shows the variation of the coupled BPPs' parameters depending on their relative position. This considers that the receiving pad moves with respect to the 3-D coordinate system in Fig. 8(a). The self-inductance is approximately constant in the x- and y-directions, while it decreases by up to 5% in the z-direction. The cross-coupling within the same pad, namely M_{12} and M_{34}, stays roughly constant with any misalignment, making it suitable to use the compensation capacitance to compensate for that. This intuitively makes sense since those coils do not change their position with respect to each other. On the other hand, the diagonal cross-coupling between opposite BPPs, namely M_{14} and M_{23}, is more sensitive to misalignment. The misalignment in the y- and z-direction results in negligible M_{14} and M_{23} since they are still lower than $(1/10) \cdot M_{24}$. On the other hand, the misalignment in the x-direction influence greatly the value of M_{14} and M_{23}. For example, shifting the receiving pad along the positive x-direction results in a drop of M_{14} whereas M_{23} increases. This is because the coil with L_4 inductance moves further away from the coil with L_1 inductance while the coil with L_3 inductance becomes

Authorized licensed use limited to: TU Delft Library. Downloaded on August 21,2023 at 13:07:11 UTC from IEEE Xplore. Restrictions apply.

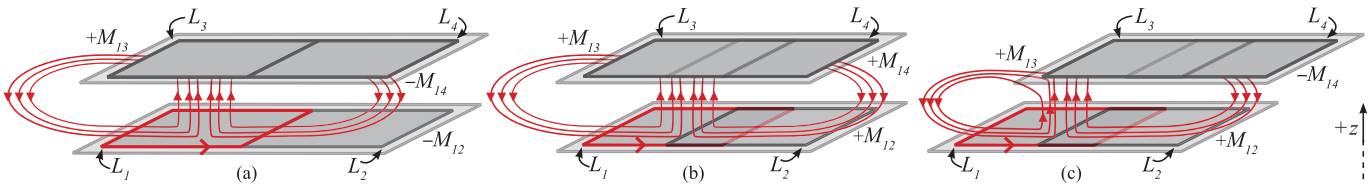

Fig. 6. Typical magnetic flux generated by a current flowing through the coil with L_1 inductance. The mutual inductance can have either a positive or negative sign depending on the direction of the field linking to the other coils. Examples for (a) aligned BPPs and $x_{\text{overlap}} = 0$, (b) aligned BPPs and $x_{\text{overlap}} > 0$, and (c) BPPs misaligned in the positive x-direction and $x_{\text{overlap}} > 0$.

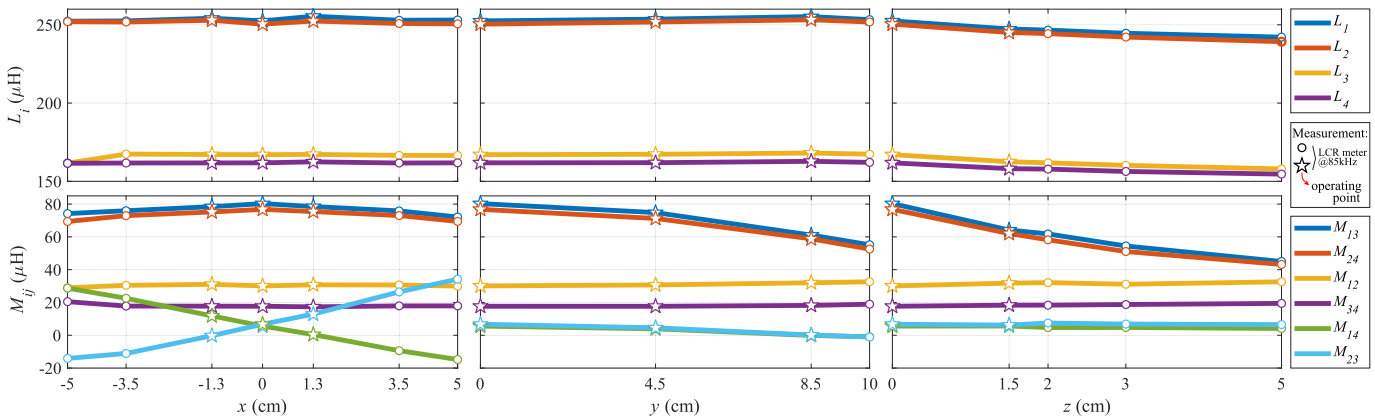

Fig. 7. Self-inductance and mutual inductance of the coupled BPPs depending on receiving pad position, measured with an LCR meter at 85 kHz. The coordinate reference system is shown in Fig. 8. Note that the misalignment is performed only with respect to one axis at a time.

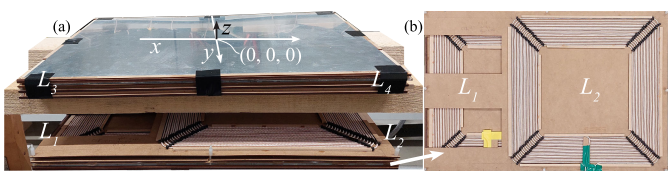

Fig. 8. Implementation of the selected BPPs design whose parameters are listed in Table IV. (a) Coupled BPPs, and (b) top view of the primary BPP.

more aligned to the coil with L_2 inductance. For misalignment points greater than 1.3 cm, M_{14} assumes a negative value. The physical reason for that is illustrated in Fig. 6(c), where it is clear that a negative magnetic flux might be concatenated to the coil with L_4 inductance when the receiving pad moves in the positive x-direction. Due to the symmetry of the BPPs, similar considerations can be made for the movement of the receiving pad along the negative x-direction.

IV. Laboratory Prototype

The equipment and the 7.7 kW implemented laboratory prototype in Fig. 9 have been used to prove the functionality of the V/I-D converter employing the BPPs in Fig. 8. One bidirectional power supply has been used as the input voltage source, mimicking the voltage from a single-phase boost-like power factor correction (PFC) rectifier connected to the European grid, which range is 360–500-V dc and could be implemented as explained in [30] and [31]. A second power supply has been employed as the load emulating the EV battery in the voltage ranges 300–400 V and 600–800 V, proving that the proposed method applies to a wide range of battery voltages and not only to 400 and 800 V ones.

TABLE V

Selected Series Compensation Capacitors for the Circuit in Fig. 1. The Values Have Been Measured With an LCR Meter at 85 kHz

Parameter	Connected to:	Value	(series x parallel)*
C_1	L_1	14.9 nF	4 x 18
C_2	L_2	14.9 nF	4 x 18
C_3	L_3	20.7 nF	4 x 25
C_4	L_4	21.6 nF	4 x 26

*Unit capacitor: KEMET R76TF13305050J 3.3 nF (ESR=0.22 Ω)

A. Compensation Capacitors' Selection

According to the cross-coupling compensation strategy explained in Section III-B, each series compensation capacitance must be computed from (9) considering $f_0 = 90$ kHz such that the cross-coupling within the same BPP is compensated for the current doubler mode. The case in which the BPPs are aligned has been considered for the calculation. In addition, the absolute value of the currents mentioned in (9) can be computed from (2) by setting all the cross-coupling terms to zero. The resulting compensation capacitances and their implementation are listed in Table V.

B. Analysis of the Operating Points

Before validating the proposed V/I-D converter experimentally, the operating points corresponding to the different BPPs alignments have been analyzed through the analytical model defined in Section II-B at the rated output power of 7.2 kW. Hereby, V_{in} is regulated to deliver the rated output power.

In the following paragraphs, two analyses are executed. First, the advantages of adopting the switching frequency of 79 kHz in the voltage doubler mode are proved against the

Authorized licensed use limited to: TU Delft Library. Downloaded on August 21,2023 at 13:07:11 UTC from IEEE Xplore. Restrictions apply.

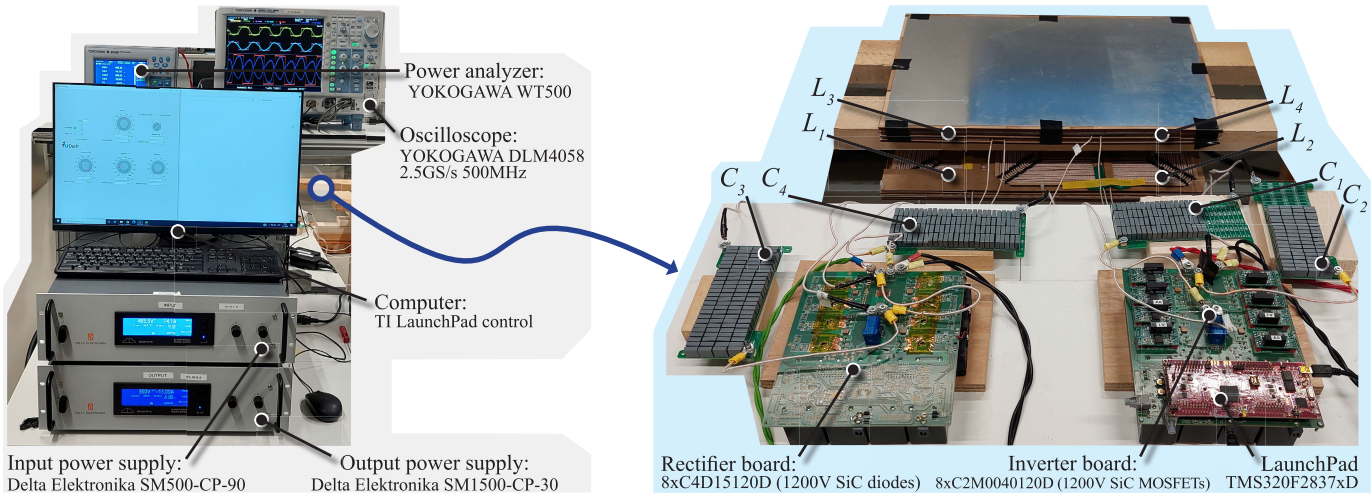

Fig. 9. Equipment and implemented 7.7-kW laboratory prototype of the V/I-D converter employing coupled BPPs.

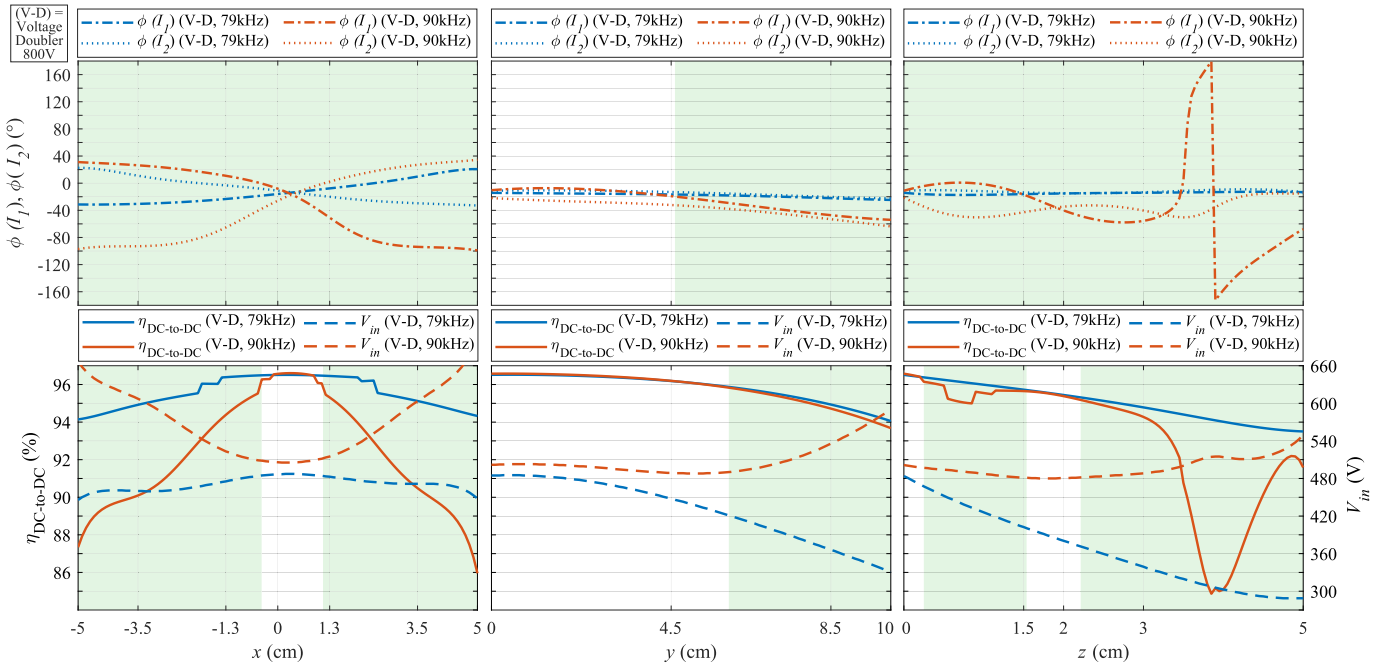

Fig. 10. Analysis from the analytical model of the proposed V/I-D converter of the phase angle of the primary currents $\phi(I_1)$ and $\phi(I_2)$, the dc-to-dc efficiency $\eta_{\text{dc-to-dc}}$, and the required input voltage V_{in} depending on the receiving coil's misalignment in the x-, y-, z-directions. The misalignment is performed only with respect to one axis at a time. The results suppose that the output power of 7.2 kW is delivered when the V/I-D converter operates as a voltage doubler, i.e., $V_{\text{out}} = 800$ V, while the inverters' switching frequency is either 79 or 90 kHz. The green-shaded areas denote the operating regions in which 79 kHz brings a considerable advantage in terms of $\eta_{\text{dc-to-dc}}$ and ZVS turn-on capability of the H-bridge inverters.

operation at 90 kHz. After that, the expected operating points are evaluated the voltage and the current doubler modes.

1) Voltage Doubler Mode Operating at Either 79 or 90 kHz: The operating points resulting from the two switching frequencies of the voltage doubler mode are summarized in Fig. 10, where the BPPs alignments in Fig. 7 have been considered. At the aligned position, the operating points from the two switching frequencies are similar. However, when the misalignment occurs, the phase angle of the primary currents $\phi(I_1)$ and $\phi(I_2)$ is lower when operating at 79 kHz than at 90 kHz. This translates into less circulating reactive current, lower switching losses of the H-bridge inverters, lower required V_{in}, and consequently, higher $\eta_{\text{dc-to-dc}}$. Note that the sharp decreases in $\eta_{\text{dc-to-dc}}$ correspond to transitions into hard-switching operating areas. In addition, it must be considered that the V_{in} required from the operation at 90 kHz could be up to 600 V. Since this is considerably higher than the maximum voltage achievable from the PFC rectifier, an extra voltage boost stage would be required to supply the H-bridge inverters adding cost and complexity. These results confirm that operating the V/I-D converter at 79 kHz is advantageous in the voltage doubler mode.

2) Voltage Doubler Mode Operating at 79 kHz and Current Doubler Mode Operating at 90 kHz: The operating points resulting from both the voltage doubler and the current doubler modes are shown in Fig. 11. According to $\phi(I_1)$ and $\phi(I_2)$, the misalignment of the receiving BPP in the x-direction pushes one primary current into the capacitive region leading to the hard-switching of the respective H-bridge inverter. Those operating points have been marked with red-shaded areas. At the

Authorized licensed use limited to: TU Delft Library. Downloaded on August 21,2023 at 13:07:11 UTC from IEEE Xplore. Restrictions apply.

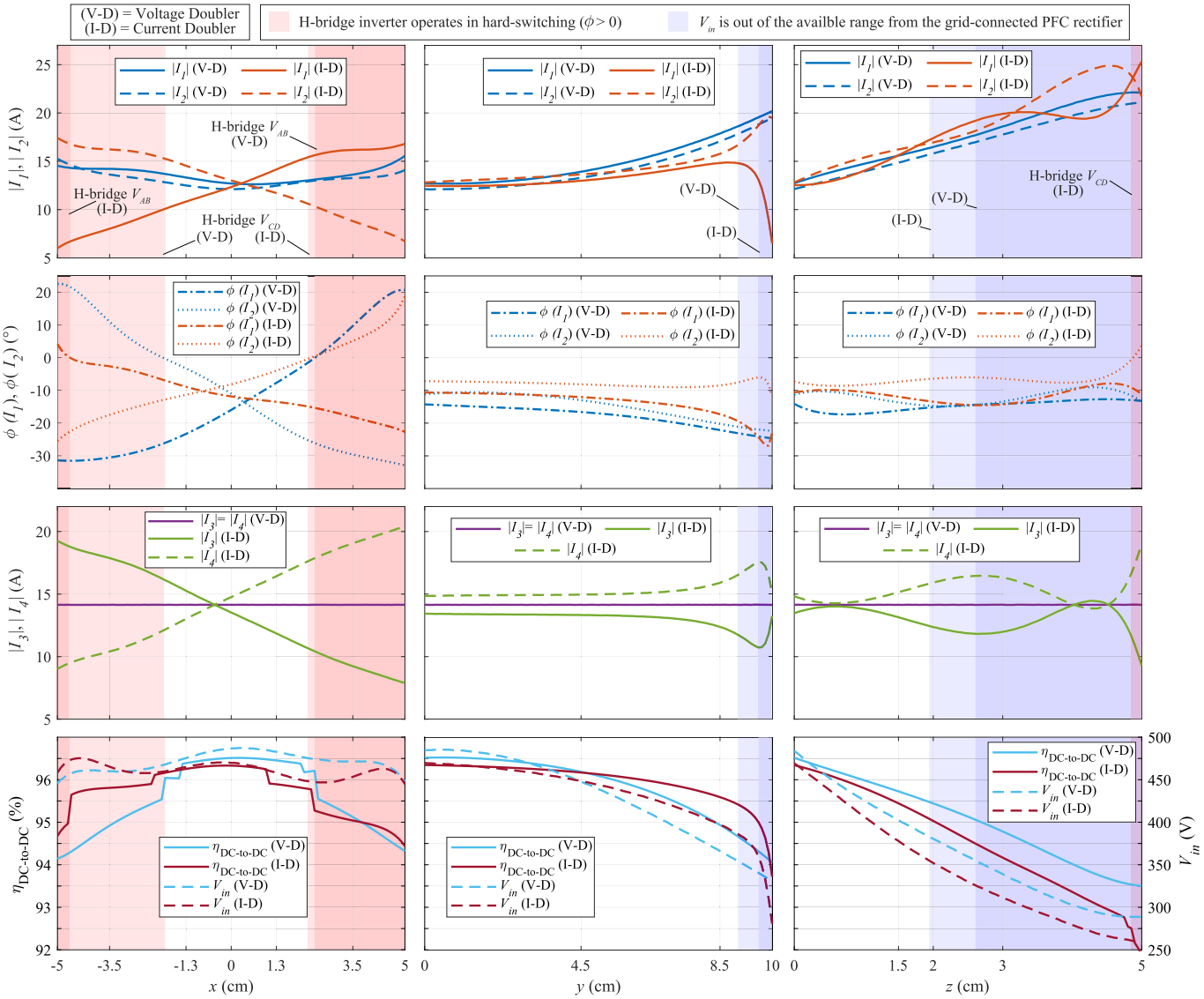

Fig. 11. Analysis from the analytical model of the proposed V/I-D converter of the absolute value and phase angle of $\boldsymbol{I_1}$ and $\boldsymbol{I_2}$, the absolute value of $\boldsymbol{I_3}$ and $\boldsymbol{I_4}$, the $\eta_{\text{dc-to-dc}}$, and the required V_{in} depending on the misalignment in the x-, y-, and z-direction. The misalignment is performed only with respect to one axis at a time. The results suppose that the output power of 7.2 kW is delivered when the V/I-D converter operates as either voltage doubler ($V_{\text{out}} = 800$ V, 79 kHz) or current doubler ($V_{\text{out}} = 400$ V, 90 kHz). The red-shaded areas denote the operating regions in which the hard-switching of the H-bridge inverter occurs. The blue-shaded areas indicate whether the required V_{in} is out of the available range from the grid-connected PFC rectifier.

same time, the other primary current becomes more inductive, causing higher turn-off losses. In addition, during the current doubler mode, the current stress in the two primary and the two secondary circuits would be unbalanced. This asymmetrical behavior is due to the opposite trend of the diagonal cross-coupling M_{14} and M_{23} with respect to the misalignment in the x-direction shown in Fig. 7. As a result, the $\eta_{\text{dc-to-dc}}$ could drop by up to 2% from the aligned case, which is still reasonable. Nevertheless, the MOSFETs of the inverting stages must be equipped with a suitable thermal management system to be able to withstand the additional power losses introduced by the hard-switching operating points. It must also be noted that the required V_{in} would still be within the available range from the grid-connected PFC rectifier. These results make the proposed V/I-D converter with BPPs more suitable for applications with a moderate misalignment profile in the x-direction. This is generally the case of EV static wireless charging since the BPPs misalignment would be constrained by the lateral size of the parking spot.

Moreover, Fig. 11 shows that the proposed V/I-D converter with BPPs has good misalignment tolerance with respect to the y-direction since the ZVS turn-on would still be preserved. However, beyond a certain extent of misalignment, the required V_{in} is lower than the minimum available (360 V) from the PFC rectifier. This occurs in the operating points marked with the blue-shaded areas in Fig. 11, which correspond to $y > 8.8$ cm for the voltage doubler mode, while the range $y > 9.6$ cm holds for the current doubler mode. In those operating points, lower input voltage values can be achieved by phase shifting the H-bridge inverter resulting in a lower fundamental component of $\boldsymbol{V}_{\text{AB}}$ and $\boldsymbol{V}_{\text{CD}}$. For the considered misalignment, the $\eta_{\text{dc-to-dc}}$ would drop by up to 2%

Authorized licensed use limited to: TU Delft Library. Downloaded on August 21,2023 at 13:07:11 UTC from IEEE Xplore. Restrictions apply.

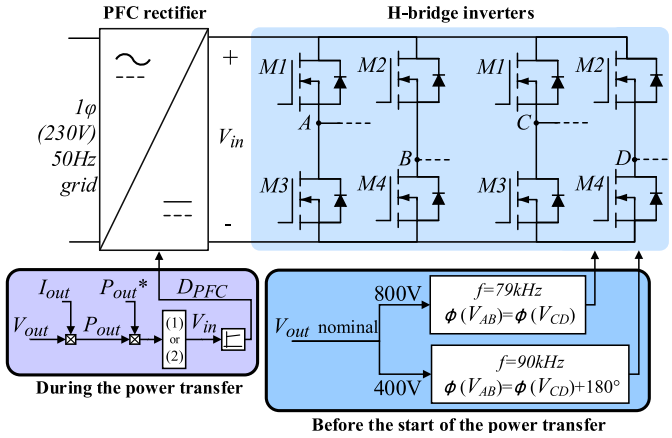

Fig. 12. Control scheme of the proposed V/I-D converter with BPPs in Fig. 1, before the start of the power transfer and during the power transfer. In the prototype of Fig. 9, the operation of the PFC rectifier is modeled by the input dc power supply.

since the same output power is reached with higher primary currents.

Similar phase shift control of the H-bridge inverters is required for a certain extent of misalignment in the z-direction, which ranges are $z > 1.9$ cm for the current doubler mode and $z > 2.5$ cm for the voltage doubler mode. This is due to the relatively high sensitivity of the main mutual inductances M_{13} and M_{24} with respect to the misalignment in the z-direction. In this case, the ZVS turn-on of the inverters would be preserved in most operating points. In addition, the $\eta_{\text{dc-to-dc}}$ could drop by up to 4% since the same output power is reached with higher primary currents.

C. Detailed Control Scheme for the V/I-D Converter With BPPs

The power transfer control scheme of the V/I-D converter is summarized in Fig. 12.

Before the start of the power transfer, the voltage doubler or current doubler operating mode is selected based on the EV battery's nominal voltage. For instance, the voltage doubler mode is suitable for batteries with 800-V nominal voltage. In this case, the H-bridge inverters are controlled to operate in phase with a 50% duty cycle at the switching frequency of 79 kHz. On the other hand, the current doubler mode is suitable for batteries with 400 V nominal voltage. The H-bridge inverters are controlled to operate 180° out of phase with a 50% duty cycle at the switching frequency of 90 kHz. The operating conditions of the H-bridge inverters are set only once before the power transfer start since the EV's battery class to be charged would be the same for the whole charging cycle.

During the power transfer, the dc input voltage V_{in} is set according to the load conditions to match the target output power P^*_{out} set by the charging cycle. The grid-connected PFC rectifier could implement this input voltage regulation. It is assumed that the information on the battery and the operating load is given by the wireless communication required from the IPT system for several features such as guided positioning, pairing, and safety.

V. Experimental Results

Based on the analysis of the operating points executed in Fig. 11, the proposed V/I-D converter in Fig. 9 has been tested with aligned and misaligned BPPs.

A. Measured Efficiency and Circuit Waveforms

Fig. 13 shows the measured $\eta_{\text{dc-to-dc}}$ and the applied V_{in} for the entire constant current (CC) charging profile at different alignment conditions of the coupled BPPs. The V/I-D converter operates in the current doubler mode at 90 kHz delivering an output current of 18 A while the output voltage varies from 300 to 400 V. On the other hand, the V/I-D converter operates in the voltage doubler mode at 79 kHz delivering an output current of 9 A while the output voltage varies from 600 to 800 V. These measurements prove the that proposed V/I-D converter is suitable for a wide range of battery voltages which do not have to be restricted necessarily to either 400 or 800 V.

The highest $\eta_{\text{dc-to-dc}}$ has been measured at aligned BPPs. For instance, at the rated power, the operation in the current doubler reached 96.34% efficiency, while 96.53% was measured during the voltage doubler mode. The difference in efficiency between the two modes is mainly because two more diodes are conducting in the current doubler mode. This high efficiency is because the primary currents have the lowest amplitude while delivering the rated output power. In addition, they have the minimum inductive behavior ensuring the ZVS turn-on of the H-bridges inverter with low turn-off losses and minimum circulating reactive current. These properties can be observed in Fig. 14, where it is also clear that the operation in the two modes is, to some extent, symmetrical, resembling the ideal operation of the V/I-D converter.

When the misalignment occurs, lower values of $\eta_{\text{dc-to-dc}}$ are measured since the required V_{in} to reach the same rated output power is generally reduced, translating into higher primary currents and, consequently, greater conduction losses. Moreover, larger asymmetries in the waveforms of the primary and secondary circuits can be noticed. For example, Fig. 15(a) and (b) show that, as expected from Fig. 11, the misalignment in the x-direction leads to a considerable difference in the phase angle of the two primary currents because of which one H-bridge is barely achieving the ZVS turn-on. Moreover, an asymmetry in the amplitude of the secondary currents can also be observed during the current doubler mode in Fig. 15(a). Overall, most of the measured $\eta_{\text{dc-to-dc}}$ are greater than 95.4% which makes the proposed V/I-D converter employing BPPs promising for EV wireless charging. The minimum $\eta_{\text{dc-to-dc}}$ of 94.83% has been measured during the voltage doubler mode at $y = +8.5$ cm. This is mainly due to the considerable circulating primary currents and the relatively high turn-off current point of the H-bridge inverters, which, as shown in Fig. 15(c) and (d), is roughly double than in the respective current doubler mode.

All considered operating points in Fig. 13 use a value of V_{in} that the grid-connected PFC rectifier could provide. Moreover, the measured circuit waveforms in both Figs. 14 and 15 show that the ZVS turn-on is guaranteed. These results agree with the ones expected from the analytical analysis in Fig. 11.

Authorized licensed use limited to: TU Delft Library. Downloaded on August 21,2023 at 13:07:11 UTC from IEEE Xplore. Restrictions apply.

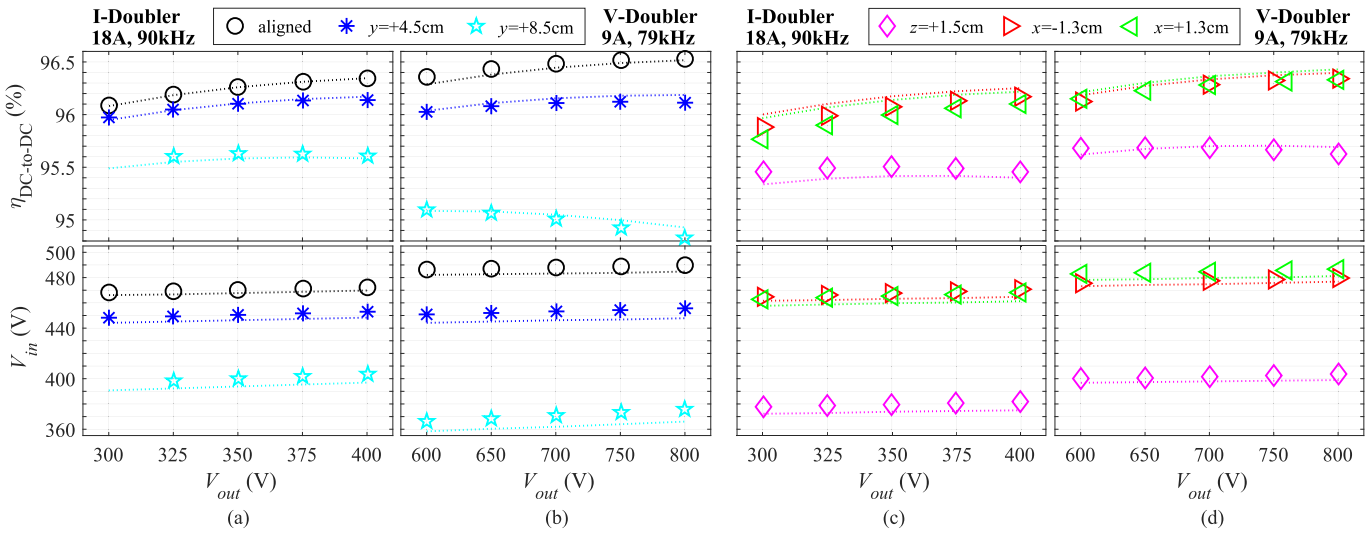

Fig. 13. Measured dc-to-dc efficiency $\eta_{\text{dc-to-dc}}$ and used input voltage V_{in} depending on V_{out} during the CC charging mode. Measurements are performed with the coupled BPPs in the aligned and the misaligned condition in the y-direction while the V/I-D converter operates as (a) current doubler and (b) voltage doubler. Measurements were performed with misaligned BPPs in either the x- or z-direction, while the V/I-D converter operates as (c) current doubler and (d) voltage doubler. Note that the misalignment is performed only with respect to one axis at a time.

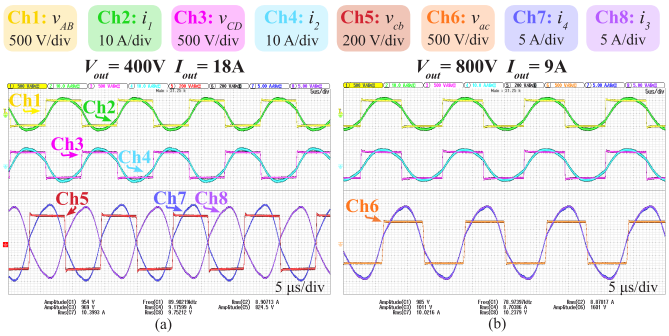

Fig. 14. Measured circuit waveforms at the nominal V_{out} and rated P_{out} when the V/I-D converter operates with aligned BPPs as (a) current doubler ($V_{\text{out}} = 400$ V) and (b) voltage doubler ($V_{\text{out}} = 800$ V).

B. Example of a CC–CV Charging Profile

Fig. 13 summarizes the measured $\eta_{\text{dc-to-dc}}$ and the applied V_{in} focusing on the CC charging profile of the EV battery since that operating mode would take place for the majority of the charging process for the rated output power level of 7.2 kW. However, the complete charging profile consisting of the CC succeeded by the constant voltage (CV) scheme can be realized by regulating the input voltage through the grid-connected PFC rectifier as shown in Fig. 12 or by the phase shift control of the H-bridge inverters.

Fig. 16 shows an example of the CC–CV charging profile realized with the proposed V/I-D converter with aligned BPPs. The measured $\eta_{\text{dc-to-dc}}$ increases during the CC charging mode, while it would drop slightly during the CV mode, where it is still higher than 96.2% for the considered operating points. All in all, Fig. 16 clearly shows that the V/I-D converter is a universal solution for efficiently charging EV batteries belonging to different voltage classes at the same power.

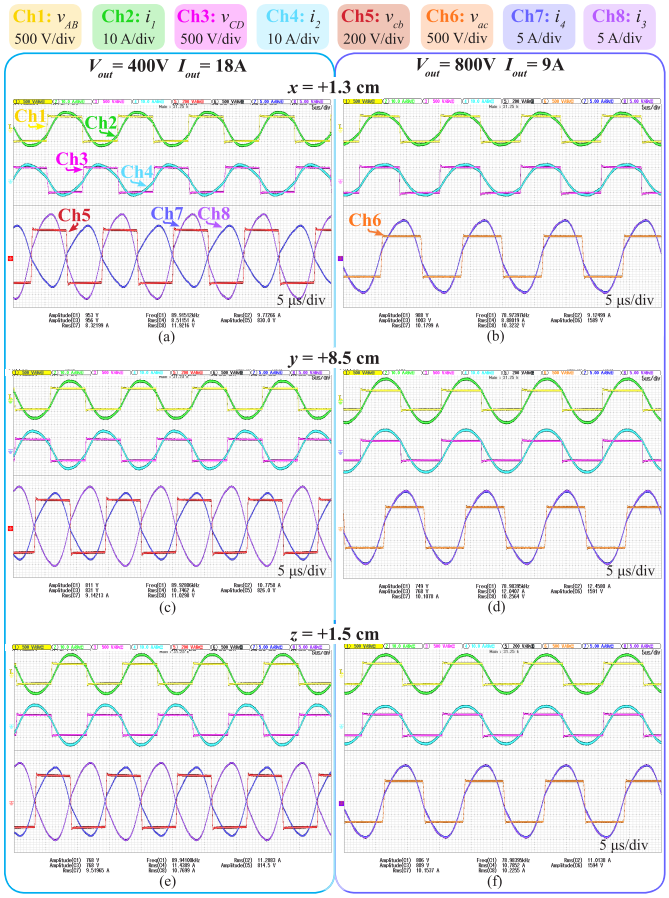

Fig. 15. Measured circuit waveforms at the nominal V_{out} and rated P_{out} when the V/I-D converter operates with misaligned BPPs as (a), (c), and (e) current doubler ($V_{\text{out}} = 400$ V) and (b), (d), and (f) voltage doubler ($V_{\text{out}} = 800$ V). The misalignment is (a) and (b) $x = 1.3$ cm, (c) and (d) $y = 8.5$ cm, and (e) and (f) $z = 1.5$ cm. The misalignment is performed only with respect to one axis at a time.

C. Performance Comparison With Other Research Works

The performance of the proposed V/I-D converter has been compared to the research works in Table VI to highlight the contributions. It can be noticed that the V/I-D converter can deliver the same output power, i.e., 7.2 kW, with nearly the same efficiency for a wide battery range. The other remarkable

Authorized licensed use limited to: TU Delft Library. Downloaded on August 21,2023 at 13:07:11 UTC from IEEE Xplore. Restrictions apply.

TABLE VI
COMPARISON OF THE PROPOSED V/I-D CONVERTER WITH TYPICAL RESEARCH WORKS FROM THE LITERATURE

Paper reference	Tx pad size (mm^2)	Rx pad size (mm^2)	Coils' air gap (mm)	Coupling factor k (p.u.)	Switching frequency (kHz)	Output power (kW)	Output voltage (V)	Measured $\eta_{DC\text{-}to\text{-}DC}$ (%)	Control only at the Tx circuit
[32]	$\pi\cdot200^2$	$\pi\cdot200^2$	125	0.20	84.6	0.3	71	96.80	✗
[25]	522x258	522x258	150	0.18	85	0.6	100	91.00	✓
[27]	450x450	450x450	150	0.36	85	3.1	354	91.29	✓
[33]	600x600	600x600	150	0.3	95	6.5	N/A	95.30	✓
[34]	625x638	440x380	167	0.2	85	7	280 420	94.00 94.20	✗
[16]	272x278	272x278	40	0.4	100	7.2	48	94.02	✓
[35]	600x800	600x800	200	0.33	79	7.7	450	96.00	✓
[36]	650x640	370x290	140	0.31	85	7.7	280 420	93 90	✓
[9]	2x387x362	2x387x362	100	0.38	86.5	7.2	400 800	97.11 97.52	✓
This paper	545x350	545x350	95	0.39	90 79	7.2	400 800	96.34 96.53	✓

Tx = transmitter, also called primary. **Rx** = receiver, also called secondary.

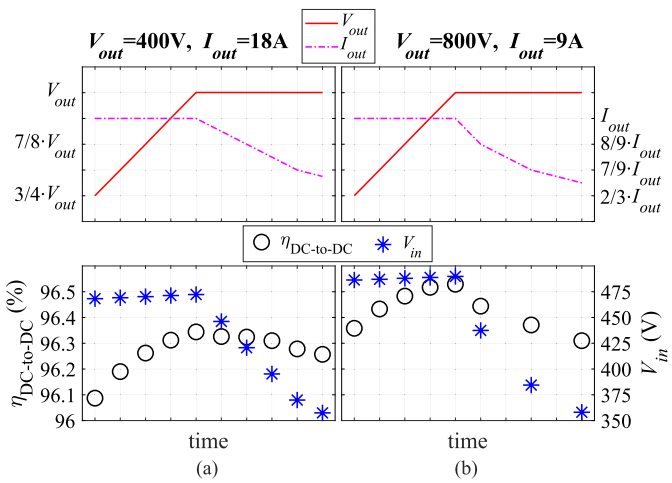

Fig. 16. Measured $\eta_{dc\text{-}to\text{-}dc}$ and used V_{in} during a typical battery charging profile with the CC and the CV modes at aligned BPPs while the V/I-D converter operates as (a) current doubler and (b) voltage doubler. These results summarize that the V/I-D converter is a universal solution for charging 400- and 800-V EV batteries efficiently at the same power.

advantage is that the power transfer control is only performed at the transmitting circuit, while the receiving circuit on board the EV conveniently consists of passive devices. Moreover, the measured dc-to-dc efficiency is higher than in the other research works.

It must be noted that the measured peak efficiency at aligned BPPs is lower than the one in [9] mainly because of the power losses due to the eddy currents in the BPPs' aluminum shield, which was not used for the separated rectangular coils. In addition, the V/I-D converter with BPPs is significantly more compact than the implementation with separated rectangular coils, resulting in less required mounting space, which is a great advantage from the industrial point of view.

VI. CONCLUSION

This article has proposed, analyzed, and experimentally verified a novel universal solution for wireless charging of EVs, which can efficiently provide the same power level to both 400- and 800-V batteries without affecting the current rating of the converter's circuit components. The proposed V/I-D converter uses series-compensated BPPs for both the transmitting and the receiving circuits, of which each coil is connected to a dedicated H-bridge. The power-flow control is performed only at the source side, which simplifies the circuit onboard the EV. The V/I-D converter has two operating modes. The voltage doubler mode is suitable to charge 800-V batteries, while the current doubler mode is suitable to charge 400 V one. The equivalent circuit of both operating modes has been modeled analytically. Additionally, an extensive analysis of the undesired cross-coupling between the two BPPs has been performed to evaluate how it impacts the power transfer. It has been found that it is preferable to design the coils' overlap area such that the diagonal cross-coupling between opposite BPPs is negligible. On the other hand, the effect of the cross-coupling between the two coils in the same BPP can be compensated by selecting the compensation capacitances. The functionality of the converter has been tested experimentally with a laboratory demonstrator at different coils' alignments in the x-, y-, and z-directions, and for load conditions typical of EV charging profiles. At 7.2 kW and with aligned BPPs, the dc-to-dc efficiency of 96.34% and 96.53% has been measured at 400 and 800 V, respectively. High efficiency and the ZVS turn-on of the H-bridge inverters are maintained throughout most operating conditions. The misalignment concerning the lateral x-direction results in the most critical operating conditions since it causes an unbalance between the two diagonal mutual inductances, eventually leading to the hard-switching of one H-bridge inverter. Nevertheless, the power transfer efficiency is expected to be higher than 94% for a misalignment in the x-direction up to ±5 cm, typical of static EV wireless charging. These measurements have considered voltage ranges 300–400 V and 600–800 V, proving that the proposed method applies to a wide range of battery voltages and not only to 400 and 800 V ones.

Authorized licensed use limited to: TU Delft Library. Downloaded on August 21,2023 at 13:07:11 UTC from IEEE Xplore. Restrictions apply.

ACKNOWLEDGMENT

We would like to acknowledge that an international patent was filed in February 2023 based on the work presented in this paper. The patent application number is PCT/NL2023/050094.

REFERENCES

[1] ZVEI-German Electrical and Electronic Manufacturers' Association Centre. (2013). *Voltage Casses for Electric Mobility*. [Online]. Available: https://www.zvei.org/fileadmin/user_upload/Presse_und_Medien/Publikationen/2014/april/Voltage_Classes_for_Electric_Mobility/Voltage_Classes_for_Electric_Mobility.pdf

[2] H. K. Bai et al., "Charging electric vehicle batteries: Wired and wireless power transfer: Exploring EV charging technologies," *IEEE Power Electron. Mag.*, vol. 9, no. 2, pp. 14–29, Jun. 2022.

[3] C. Jung, "Power up with 800-V systems: The benefits of upgrading voltage power for battery-electric passenger vehicles," *IEEE Electrific. Mag.*, vol. 5, no. 1, pp. 53–58, Mar. 2017.

[4] I. Aghabali, J. Bauman, P. J. Kollmeyer, Y. Wang, B. Bilgin, and A. Emadi, "800-V electric vehicle powertrains: Review and analysis of benefits, challenges, and future trends," *IEEE Trans. Transport. Electrific.*, vol. 7, no. 3, pp. 927–948, Sep. 2021.

[5] D.-W. Lee, B.-S. Lee, J.-H. Ahn, J.-Y. Kim, and J.-K. Kim, "New combined OBC and LDC system for electric vehicles with 800 V battery," *IEEE Trans. Ind. Electron.*, vol. 69, no. 10, pp. 9938–9951, Oct. 2022.

[6] *EVSpecifications*. Accessed: Oct. 5, 2022. [Online]. Available: https://www.evspecifications.com/

[7] *J2954: Wireless Power Transfer for Light-Duty Plug-In/ Electric Vehicles and Alignment Methodology*, SAE Int. Std., Warrendale, PA, USA, Aug. 2022.

[8] F. Grazian, W. Shi, J. Dong, P. van Duijsen, T. B. Soeiro, and P. Bauer, "Survey on standards and regulations for wireless charging of electric vehicles," in *Proc. AEIT Int. Conf. Electr. Electron. Technol. Automot. (AEIT AUTOMOTIVE)*, 2019, pp. 1–5.

[9] F. Grazian, T. B. Soeiro, and P. Bauer, "Voltage/current doubler converter for an efficient wireless charging of electric vehicles with 400-V and 800-V battery voltages," *IEEE Trans. Ind. Electron.*, vol. 70, no. 8, pp. 7891–7903, Aug. 2022.

[10] G. A. Covic, M. L. G. Kissin, D. Kacprzak, N. Clausen, and H. Hao, "A bipolar primary pad topology for EV stationary charging and highway power by inductive coupling," in *Proc. IEEE Energy Convers. Congr. Exposit.*, Sep. 2011, pp. 1832–1838.

[11] M. Budhia, J. T. Boys, G. A. Covic, and C.-Y. Huang, "Development of a single-sided flux magnetic coupler for electric vehicle IPT charging systems," *IEEE Trans. Ind. Electron.*, vol. 60, no. 1, pp. 318–328, Jan. 2013.

[12] T. F. Wu, C. T. Tsai, Y. D. Chang, and Y. M. Chen, "Analysis and implementation of an improved current-doubler rectifier with coupled inductors," *IEEE Trans. Power Electron.*, vol. 23, no. 6, pp. 2681–2693, Nov. 2008.

[13] C. H. Kwan, J. M. Arteaga, N. Pucci, D. C. Yates, and P. D. Mitcheson, "A 110W E-scooter wireless charger operating at 6.78 MHz with ferrite shielding," in *Proc. IEEE PELS Workshop Emerg. Technol., Wireless Power Transf. (WoW)*, Jun. 2021, pp. 1–4.

[14] H. Z. Beh, M. Neath, J. T. Boys, and G. A. Covic, "An alternative IPT pickup controller for material handling using a current doubler," *IEEE Trans. Power Electron.*, vol. 33, no. 12, pp. 10135–10147, Dec. 2018.

[15] Y. Wang et al., "Research on 11kW wireless charging system for electric vehicle based on LCC-SP topology and current doubler," in *Proc. IEEE Energy Convers. Congr. Exposit. (ECCE)*, Oct. 2020, pp. 820–827.

[16] L. Shi, A. Delgado, R. Ramos, and P. Alou, "A wireless power transfer system with inverse coupled current doubler rectifier for high-output current applications," *IEEE Trans. Ind. Electron.*, vol. 69, no. 5, pp. 4607–4616, May 2022.

[17] R. L. Steigerwald, "A comparison of half-bridge resonant converter topologies," *IEEE Trans. Power Electron.*, vol. PE-3, no. 2, pp. 174–182, Apr. 1988.

[18] A. Zaheer, H. Hao, G. A. Covic, and D. Kacprzak, "Investigation of multiple decoupled coil primary pad topologies in lumped IPT systems for interoperable electric vehicle charging," *IEEE Trans. Power Electron.*, vol. 30, no. 4, pp. 1937–1955, Apr. 2015.

[19] F. Y. Lin, G. A. Covic, and J. T. Boys, "Evaluation of magnetic pad sizes and topologies for electric vehicle charging," *IEEE Trans. Power Electron.*, vol. 30, no. 11, pp. 6391–6407, Nov. 2015.

[20] F. Y. Lin, G. A. Covic, and J. T. Boys, "Leakage flux control of mismatched IPT systems," *IEEE Trans. Transport. Electrific.*, vol. 3, no. 2, pp. 474–487, Jun. 2017.

[21] F. Lin, G. A Covic, and J. T. Boys, "A comparison of multi-coil pads in IPT systems for EV charging," in *Proc. IEEE Energy Convers. Congr. Exposit. (ECCE)*, Sep. 2018, pp. 105–112.

[22] F. Lin, G. A. Covic, and M. Kesler, "Design of a SAE compliant multicoil ground assembly," *IEEE J. Emerg. Sel. Topics Ind. Electron.*, vol. 1, no. 1, pp. 14–25, Jul. 2020.

[23] A. Zaheer, D. Kacprzak, and G. A. Covic, "A bipolar receiver pad in a lumped IPT system for electric vehicle charging applications," in *Proc. IEEE Energy Convers. Congr. Exposit. (ECCE)*, Sep. 2012, pp. 283–290.

[24] A. Zaheer, G. A. Covic, and D. Kacprzak, "A bipolar pad in a 10-kHz 300-W distributed IPT system for AGV applications," *IEEE Trans. Ind. Electron.*, vol. 61, no. 7, pp. 3288–3301, Jul. 2014.

[25] N. Rasekh, J. Kavianpour, and M. Mirsalim, "A novel integration method for a bipolar receiver pad using LCC compensation topology for Wireless power transfer," *IEEE Trans. Veh. Technol.*, vol. 67, no. 8, pp. 7419–7428, Aug. 2018.

[26] H. Jafari, T. O. Olowu, M. Mahmoudi, and A. Sarwat, "Optimal design of IPT bipolar power pad for roadway-powered EV charging systems," *IEEE Can. J. Electr. Comput. Eng.*, vol. 44, no. 3, pp. 350–355, Jul. 2021.

[27] W. Zhao, X. Qu, J. Lian, and C. K. Tse, "A family of hybrid IPT couplers with high tolerance to pad misalignment," *IEEE Trans. Power Electron.*, vol. 37, no. 3, pp. 3617–3625, Mar. 2022.

[28] Y. Li, R. Mai, L. Lu, T. Lin, Y. Liu, and Z. He, "Analysis and transmitter currents decomposition based control for multiple overlapped transmitters based WPT systems considering cross couplings," *IEEE Trans. Power Electron.*, vol. 33, no. 2, pp. 1829–1842, Feb. 2018.

[29] R. Mai, Y. Luo, B. Yang, Y. Song, S. Liu, and Z. He, "Decoupling circuit for automated guided vehicles IPT charging systems with dual receivers," *IEEE Trans. Power Electron.*, vol. 35, no. 7, pp. 6652–6657, Jul. 2020.

[30] J. W. Kolar, J. Biela, and J. Minibock, "Exploring the Pareto front of multi-objective single-phase PFC rectifier design optimization -99.2% efficiency vs. 7kw/din^3 power density," in *Proc. IEEE 6th Int. Power Electron. Motion Control Conf.*, May 2009, pp. 1–21.

[31] J. Paulo M. Figueiredo, F. L. Tofoli, and B. Leonardo A. Silva, "A review of single-phase PFC topologies based on the boost converter," in *Proc. 9th IEEE/IAS Int. Conf. Ind. Appl. (INDUSCON)*, Nov. 2010, pp. 1–6.

[32] Y. Jiang, L. Wang, J. Fang, C. Zhao, K. Wang, and Y. Wang, "A joint control with variable ZVS angles for dynamic efficiency optimization in wireless power transfer system," *IEEE Trans. Power Electron.*, vol. 35, no. 10, pp. 11064–11081, Oct. 2020.

[33] W. Li, H. Zhao, S. Li, J. Deng, T. Kan, and C. C. Mi, "Integrated *LCC* compensation topology for wireless charger in electric and plug-in electric vehicles," *IEEE Trans. Ind. Electron.*, vol. 62, no. 7, pp. 4215–4225, Jul. 2015.

[34] G. R. Kalra, B. S. Riar, and D. J. Thrimawithana, "An integrated boost active bridge based secondary inductive power transfer converter," *IEEE Trans. Power Electron.*, vol. 35, no. 12, pp. 12716–12727, Dec. 2020.

[35] W. Li, H. Zhao, J. Deng, S. Li, and C. C. Mi, "Comparison study on SS and double-sided LCC compensation topologies for EV/PHEV wireless chargers," *IEEE Trans. Veh. Technol.*, vol. 65, no. 6, pp. 4429–4439, Jun. 2016.

[36] W. Victor Wang, D. J. Thrimawithana, and M. Neuburger, "An Si MOSFET-based high-power wireless EV charger with a wide ZVS operating range," *IEEE Trans. Power Electron.*, vol. 36, no. 10, pp. 11163–11173, Oct. 2021.

Authorized licensed use limited to: TU Delft Library. Downloaded on August 21,2023 at 13:07:11 UTC from IEEE Xplore. Restrictions apply.